

Real-Time Neural Hair Denoising

CHENGHAO WU*, University of Manchester, United Kingdom

YUEFAN SHEN, LIGHTSPEED, China

TAO HUANG, LIGHTSPEED, China

KAI YAN, LIGHTSPEED, China

ZAHRA MONTAZERI, University of Manchester, United Kingdom

KUI WU, LIGHTSPEED, USA

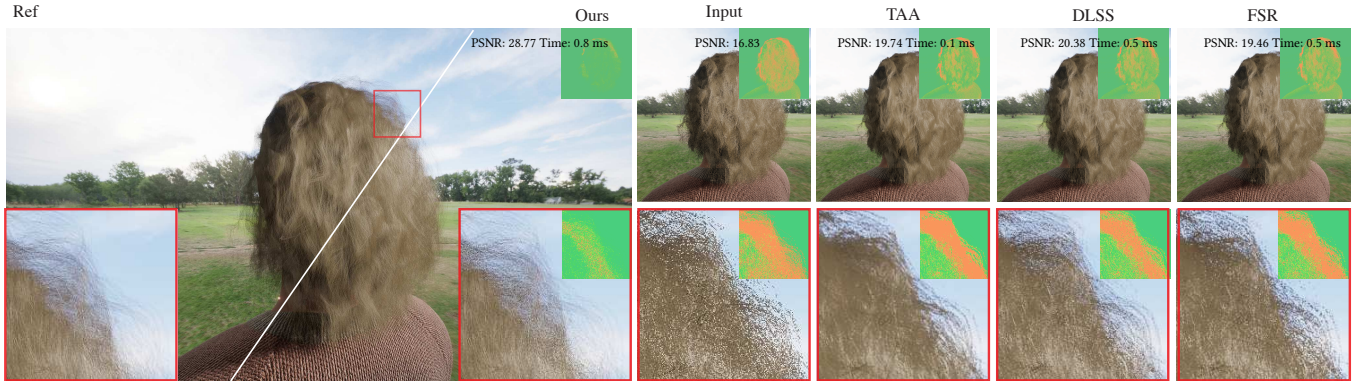


Fig. 1. We showcase the denoising results of our method given severely undersampled strand-based hair G-buffers. Compared with TAA, DLSS, and FSR, our approach better preserves sparse hair silhouettes and fine strand details, producing results closer to the high-sample reference. Insets show the corresponding error maps, and blue boxes indicate zoomed regions.

We propose a lightweight real-time method for reconstructing strand-based hair G-Buffers from severely undersampled rasterized inputs. Our pipeline first applies neural spatial reconstruction and temporal accumulation to recover hair coverage, i.e., fractional hair visibility within a pixel, and tangent. It then uses a tangent-guided reconstruction step to complete the position, which is subsequently used for physically based deferred hair shading. We evaluate our method across a diverse set of hairstyles, including straight, wavy, afro, and ponytail styles, under both static and dynamic scenarios. Our method achieves higher hair reconstruction quality than existing hair-specific denoising techniques and general industrial neural reconstruction solutions such as DLSS and FSR.

CCS Concepts: • **Computing methodologies** → **Rendering**.

1 Introduction

Hair is one of the most important visual cues for digital characters, and high-quality hair rendering has become essential in modern real-time applications, including games, virtual production, AR/VR, and social avatars. Despite its importance, hair remains challenging to render efficiently. A typical hairstyle contains tens of thousands of strands, each of which is often much thinner than a pixel at common viewing distances. As a result, hair exhibits extreme subpixel complexity and requires a large number of samples per pixel to

adequately suppress noise and aliasing. For general scenes, rasterization is usually efficient, and shading tends to be the dominant bottleneck. Hair rendering, however, is fundamentally different: rasterization itself is already expensive due to the large number of thin geometric primitives. Moreover, the extremely small screen-space footprint of individual hairs makes them highly susceptible to severe undersampling, resulting in noisy renderings. The thin and highly detailed structure of hair also makes it difficult for general anti-aliasing methods, including recent learning-based approaches such as DLSS4 [NVIDIA 2025] and FSR [AMD 2021], to handle effectively. Although recent approaches have explored hair filtering through multisample anti-aliasing on the visibility buffer [Tafari 2019], hair linking [Huang et al. 2025b], anisotropic filtering [Fu 2023], and neural filtering [Currius et al. 2022], their runtime cost still falls short of the constraints of modern game production, where the filtering stage is typically limited to only a few milliseconds.

Unlike prior work that denoises the final shaded image, where errors are already entangled with lighting, visibility, and the hair shading model, our method reconstructs low-sample rasterized hair G-buffers prior to shading. Operating in G-buffer space preserves the geometric and directional information required for physically based hair shading, enabling better temporal coherence and stronger geometric fidelity. More specifically, undersampled rasterized hair G-buffers exhibit two major failure modes. First, attributes such as coverage and tangent are sparse, aliased, and noisy. Second, geometric buffers, such as position and depth, are often incomplete, making deferred shading unstable and prone to flickering artifacts.

*This work was done when Chenghao Wu was an intern at LIGHTSPEED.

Authors' Contact Information: Chenghao Wu, chenghao.wu@manchester.ac.uk, University of Manchester, United Kingdom; Yuefan Shen, jhonve@zju.edu.cn, LIGHTSPEED, China; Tao Huang, tao_huang@ucsb.edu, LIGHTSPEED, China; Kai Yan, kyan8@uci.edu, LIGHTSPEED, China; Zahra Montazeri, zahra.montazeri@manchester.ac.uk, University of Manchester, United Kingdom; Kui Wu, walker.kui.wu@gmail.com, LIGHTSPEED, USA.

In this paper, we address these issues by proposing a novel **light-weight real-time pipeline** for **high-quality hair G-buffer reconstruction for deferred shading**. Our contributions include:

- A lightweight **spatial-temporal neural reconstruction** framework for low-sample coverage and tangent buffers, improving both reconstruction quality and temporal stability (§4).
- A **tangent-guided position completion method** that combines reconstructed coverage and tangent with noisy position and depth inputs to produce a shading-ready hair G-buffer (§5).

We evaluate our method on a diverse set of hairstyles, including straight, wavy, afro, and ponytail styles, under both static and dynamic motion (§6). Our method outperforms existing hair-specific denoising, conventional anti-aliasing, and industrial neural reconstruction baselines in hair reconstruction quality while maintaining comparable real-time performance.

2 Related work

Hair Rendering. Kajiya and Kay [1989] introduced the first physically based analytic hair shading model. This was later extended by Marschner et al. [2003] into the widely used hair BCSDf model, which decomposes scattering inside dielectric fibers into the R , TT , and TRT modes. Since then, many works have extended this model, including the addition of a diffuse term for improved data fitting [Zinke et al. 2009], artist-friendly lobe decompositions [Sadeghi et al. 2010], additional lobes for improved energy conservation and high-order scattering [Chiang et al. 2016; d’Eon et al. 2011], and extensions to elliptical hairs, animal fur, and microfacet-based scattering [Huang et al. 2022; Khungurn and Marschner 2017; Yan et al. 2015]. More recently, wave-optics models have been proposed to capture the colorful glints of hair and fur [Xia et al. 2023, 2020].

Efficient approximation of multiple scattering is critical for realistic strand-based rendering. Prior work has explored photon mapping with volumetric radiance storage [Moon and Marschner 2006; Moon et al. 2008], neural prediction of high-order scattering [KT et al. 2023], and dual scattering for real-time rendering [Yuksel and Keyser 2008; Zinke et al. 2008]. Huang et al. [2025a] further enable efficient multiple-scattering approximation with textured strand details via precomputed dual-scattering corrections.

To further accelerate rendering, aggregation models have been developed to represent clusters of fibers or hairs using coarser primitives. Koh and Huang [2001] pioneered the use of polygon strips with alpha maps to represent clusters of hair strands for real-time applications; this approach remains widely used in the game industry [Jiang 2016]. To better approximate the aggregated scattering behavior within fiber bundles, Montazeri et al. [2021, 2020] modeled woven and knitted structures using normal mapping and a specialized BSDF with separate surface and body components. Zhu et al. [2023, 2022] later introduced neural and analytical aggregated BCSDf models for fiber bundles and yarns, respectively. Bhokare et al. [2024] generated hair strand geometry on-the-fly based on *hair mesh* [Wu and Yuksel 2016; Yuksel et al. 2009], greatly reducing storage and memory bandwidth requirements for real-time hair rendering. More recently, Huang et al. [2025c] presented a real-time strand-based rendering framework with seamless level-of-detail

transitions, using an aggregated BCSDf to preserve both single- and multiple-scattering effects within hair clusters.

While many approaches have been proposed to improve the performance of strand-based rendering, including hair level-of-detail (LoD), aggregated models, and dual scattering, the intrinsic geometric nature of hair remains challenging: its width is often smaller than a screen pixel, which requires a large number of samples per pixel to achieve denoised results.

Hair Denoising. Anti-aliasing and reconstruction are fundamental problems in real-time rendering. Supersample anti-aliasing (SSAA) mitigates aliasing by full-image supersampling at high cost, whereas multisample anti-aliasing (MSAA) improves geometric edge quality while reducing shading noise. Post-process filters, such as fast approximate anti-aliasing (FXAA) [Lottes 2009], provide efficient edge smoothing but may blur fine details. Temporal methods such as temporal anti-aliasing (TAA) [Yang et al. 2020] improve both anti-aliasing and denoising through cross-frame accumulation, but can introduce ghosting under motion or disocclusion. More recently, neural reconstruction methods such as deep learning super sampling (DLSS) 4 [NVIDIA 2025] and AMD FidelityFX Super Resolution (FSR) [AMD 2021] have combined temporal information with learned super-resolution to improve image quality. However, while these techniques work well for general geometry, they are less effective for high-frequency structures such as hair, where aliasing artifacts can persist even after edge detection and filtering.

In strand-based hair rendering, simply enabling MSAA is insufficient to eliminate aliasing and also increases rendering cost due to severe overdraw. To address this, the industrial solution [Tafari 2019] adopts a pipeline in which all hair strands are first rasterized in a lightweight MSAA pass into the visibility buffer and then processed by a sample deduplication, so that only distinct samples within each pixel are shaded to produce the anti-aliased result. This pipeline has been widely adopted in modern game engines [Epic Games 2021; Kulikov 2015]. Fu [2023] proposed an elliptical kernel designed to suppress noise while preserving fine strand detail. In both industry and academia, general Monte Carlo denoising has been extensively studied using learning-based approaches, including robust average networks [Kalojanov and Thurston 2023]. For hair-specific reconstruction, Currius et al. [2022] presented a CNN-based method that uses color, specular, alpha, depth, and tangent features to reconstruct hair color, specular, and alpha, but it suffers from blurring, energy variation, and high inference cost. In contrast, our method employs a lightweight network to directly denoise the tangent and coverage and fill position based on them in the G-buffer, yielding better visual quality with lower runtime overhead.

3 Overview

As errors in the final shaded image are already entangled with lighting, visibility, and material response, making them difficult to correct consistently, our goal is to recover a temporally stable and geometrically consistent hair representation from severely undersampled rasterized G-buffers that preserves the underlying geometric and directional structure needed for physically-based hair shading. By restoring reliable intermediate attributes before shading, we can better preserve both temporal coherence and geometric fidelity.

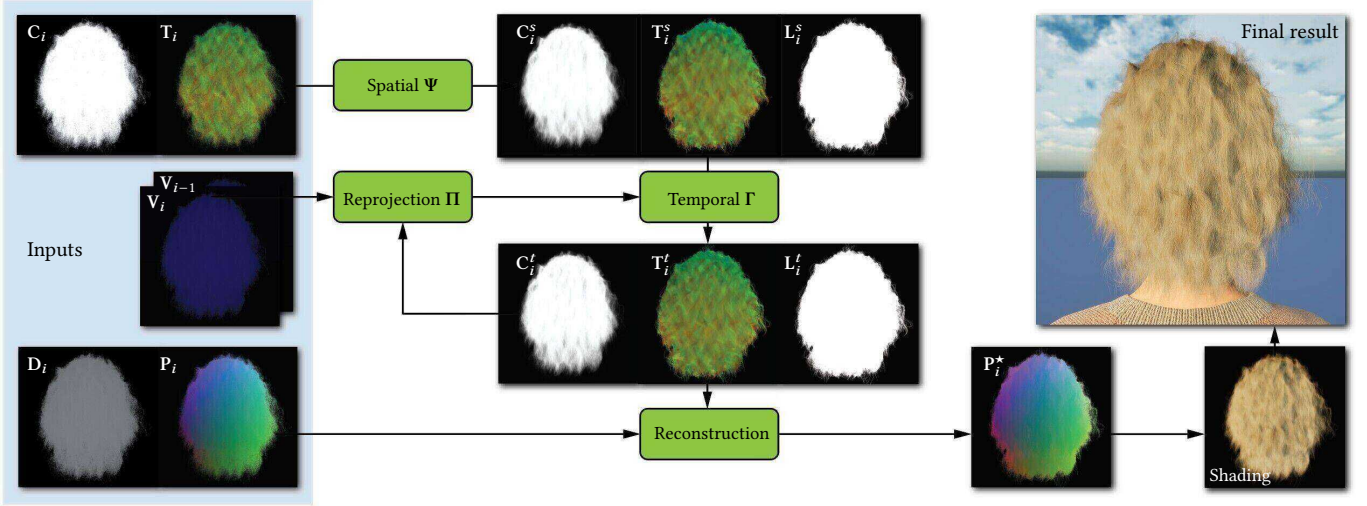


Fig. 2. The pipeline of our neural hair denoiser. Starting from low-sample, aliased hair renderings, we extract noisy hair G-buffers, including coverage C_i , tangent T_i , position P_i , and depth D_i . A spatiotemporal neural denoiser is applied to tangent and coverage through a spatial module Ψ and a temporal module Γ , while the noisy depth and position are directly fed into the reconstruction stage. Using consecutive noisy tangent and coverage inputs and motion vectors V_i and V_{i-1} , the neural denoiser provides a recurrent feedback loop from the current frame to the next. With the denoised tangent and coverage, together with the original noisy depth and position, our method reconstructs the hair position P_i^* and completes the hair G-buffer. The reconstructed G-buffer is then used for deferred hair shading, producing a high-quality final image from sparse input samples.

At low sample counts, rasterized hair G-buffers exhibit two major failure modes. First, per-pixel coverage and tangent are sparse, aliased, and noisy. Second, geometric buffers such as position and depth are often incomplete, which in turn makes deferred shading unstable and prone to flickering artifacts. Among these attributes, coverage and tangent are relatively amenable to neural prediction, since they are locally correlated and can often be inferred from nearby strand patterns in screen space. In contrast, position and depth are more difficult to predict directly, as they require stronger geometric consistency and are highly sensitive to occlusion and missing samples. To address these issues, we propose a hybrid neural-analytic reconstruction pipeline that restores reliable hair attributes before deferred shading. As shown in Fig. 2, the pipeline consists of four stages: neural spatial reconstruction of hair coverage and tangent (§4.1), neural temporal accumulation of the reconstructed coverage and tangent (§4.2), analytic tangent-guided reconstruction of position and completion of the G-buffer (§5), and physically-based deferred hair shading. Our whole pipeline can be seamlessly integrated into the current industrial game engine.

4 Neural Prediction

The neural prediction restores the two most critical hair attributes for subsequent geometric completion: coverage and tangent. We decompose this into a per-frame spatial reconstruction module and a recurrent temporal accumulation module, each with distinct characteristics: the spatial module learns to repair aliasing and local corruption within a single frame, while the temporal module learns to accumulate information over time and suppress flicker under motion and disocclusion. Both modules are trainable components. The first is a lightweight dual-branch U-Net, denoted by Ψ , which

operates on a single frame. The second is a compact recurrent convolutional module, denoted by Γ , which refines the spatial predictions using reprojected temporal history.

4.1 Spatial Reconstruction

For each frame i , the spatial module takes as input the 4-channel tensor $X_i = [C_i, T_i] \in \mathbb{R}^{H \times W \times 4}$, where $C_i \in \mathbb{R}^{H \times W \times 1}$ is the noisy coverage buffer and $T_i \in \mathbb{R}^{H \times W \times 3}$ is the noisy tangent buffer encoded in three channels. The spatial network predicts $S_i = \Psi(X_i) = [C_i^s, T_i^s, L_i^s] \in \mathbb{R}^{H \times W \times 5}$, where C_i^s is the reconstructed coverage, T_i^s is the reconstructed tangent, and L_i^s is a foreground support-mask logit, used to suppress unreliable predictions outside the hair region. We demonstrate the network architecture of our neural denoiser in the supplementary material.

Dual-branch Spatial Encoder. As coverage and tangent have different statistics: coverage is scalar and sparse, while tangent is vector-valued and locally directional, we process them using separate shallow encoder branches before fusion. A 3×3 convolution maps the coverage channel to $N = 32$ feature channels, and a second 3×3 convolution maps the 3-channel tangent input to N feature channels. Each branch then applies two encoder stages. Each stage consists of residual convolutional blocks followed by a stride-2 3×3 convolution for downsampling. The feature dimensions follow $N \rightarrow 2N \rightarrow 4N$, with corresponding spatial resolutions $H \times W, \frac{H}{2} \times \frac{W}{2}, \frac{H}{4} \times \frac{W}{4}$. Each residual block comprises two standard 3×3 convolutions with batch normalization and ReLU activations, followed by an identity skip connection. We use standard convolutions rather than depthwise separable convolutions, since the relatively small channel counts in our setting are more efficiently handled by dense convolution kernels on modern GPUs.

Bottleneck Fusion and Self-attention. At the bottleneck, the coverage and tangent features are concatenated to form an $8N$ -channel representation at resolution $\frac{H}{4} \times \frac{W}{4}$. This fused representation is processed by additional residual blocks followed by a multi-head self-attention module. The attention block uses GroupNorm pre-normalization, 1×1 convolutional projections for queries, keys, and values, four attention heads, and a feed-forward network composed of two 1×1 convolutions with GELU activation and expansion ratio 2. The bottleneck resolution is sufficiently small that global attention remains affordable while still enabling long-range interactions across hair structures. This is particularly useful for sparse hair input, where valid local evidence may be weak, but consistent larger-scale flow patterns remain. When available, we use FlashAttention [Dao et al. 2022] to reduce memory overhead.

Decoder and Skip Connections. The decoder mirrors the encoder with two upsampling stages. Each stage performs bilinear upsampling followed by a 1×1 convolution that halves the number of channels. The encoder features from the corresponding coverage and tangent branches are concatenated and fused into the decoder through skip connections. This design reintroduces high-frequency spatial detail while avoiding the larger memory cost of fully concatenating all decoder features. A final 3×3 convolution produces the output tensor.

Hierarchical Filtering Branch. In parallel with the main residual decoder, we introduce a lightweight multi-scale filtering branch that provides a low-frequency denoised estimate of the input. This branch is inspired by multi-scale kernel-predicting denoisers [Vogels et al. 2018], but instead of predicting dense per-pixel spatial kernels, it predicts compact channel-wise filtering coefficients and blending weights, to achieve the fast inference speeds required for real-time performance. At the bottleneck and the first decoder level, a 1×1 convolution predicts four sigmoid-normalized filtering coefficients κ^l , one for each channel of the coverage-tangent input, together with a sigmoid-normalized blending coefficient β^l :

$$[\kappa^l, \beta^l] = K^l(F^l), l \in \{4\times, 2\times\}, \quad (1)$$

where F^l is the corresponding bottleneck or decoder feature map, and K^l is implemented as a 1×1 convolution. These coefficients are applied element-wise to average-pooled input buffers:

$$H^l = \kappa^l \odot X^l, \quad (2)$$

where \odot denotes element-wise multiplication, X^l is the 4-channel input at scale l . The coarse $4\times$ estimate is first upsampled and blended with the finer $2\times$ estimate:

$$H_{\text{fused}}^{2\times} = (1 - \text{up}(\beta^{4\times})) \odot H^{2\times} + \text{up}(\beta^{4\times}) \odot \text{up}(H^{4\times}). \quad (3)$$

The fused estimate is then upsampled to full resolution and modulated by the decoder-level blending coefficient:

$$H = \text{up}(H_{\text{fused}}^{2\times}) \odot \text{up}(\beta^{2\times}). \quad (4)$$

This auxiliary branch provides an adaptive low-frequency prior that stabilizes the residual reconstruction path. Operator $\text{up}(\cdot)$ denotes bilinear upsampling.

Spatial Output Head. Let $R_i \in \mathbb{R}^{H \times W \times 4}$ denote the residual predicted for coverage and tangent, and H_i denote the filtered estimate from the hierarchical branch. The spatial output is formed as

$$Z_i = X_i + sR_i + H_i, \quad (5)$$

where s is a learned scalar residual scale.

4.2 Temporal Accumulation

Although the spatial module improves per-frame quality, its predictions may still flicker because sparse rasterization artifacts vary across frames. We therefore introduce a recurrent temporal module that refines the current spatial prediction using reprojected history. Let Y_{i-1} denote the previous temporal output. For frame i , we reproject Y_{i-1} into the current frame using the current motion vector V_i . We also compute a warped motion vector difference $\Delta V_i = V_i - \Pi(Y_{i-1}, V_i)$, where $\Pi(\cdot)$ denotes bilinear reprojection using motion vectors. This term provides a local cue for motion inconsistency, acceleration, and disocclusion [Edison and Jiji 2017]. Note that obtaining the motion vectors incurs no additional computational cost, as they are already provided by the standard rendering pipeline by default. The temporal input is

$$U_i = [S_i, \Pi(Y_{i-1}, V_i), V_i, \Delta V_i] \in \mathbb{R}^{H \times W \times 14}. \quad (6)$$

The channel count is therefore $14 = 5 + 5 + 2 + 2$. On the first frame of a sequence, or whenever valid history is unavailable, we set the reprojected history and the motion-vector difference to zero.

The temporal module Γ is implemented as a compact residual CNN. A 3×3 convolution maps the 14-channel input to 32 hidden channels, followed by batch normalization and ReLU. This is followed by 4 residual blocks and a final 3×3 convolution that predicts a 5-channel residual correction:

$$[\Delta C_i, \Delta T_i, \Delta L_i] = \Gamma(U_i). \quad (7)$$

The final temporal prediction is formed as

$$[C_i^t, T_i^t, L_i^t] = [C_i^s, T_i^s, L_i^s] + \alpha[\Delta C_i, \Delta T_i, \Delta L_i], \quad (8)$$

where α is a learned residual scale initialized to a small value. If I_i indicates that the current frame is the first frame in a sequence, the temporal module directly returns the spatial prediction, preventing invalid history from corrupting the output. During inference, we threshold the support mask derived from L_i and use it to suppress coverage and tangent predictions outside the reconstructed hair support. The resulting 5-channel tensor $Y_i = [C_i^t, T_i^t, L_i^t]$ is then stored as recurrent history for the next frame.

4.3 Two-Stage Training

We train the spatial and temporal modules in two stages. In the first stage, only the spatial network Ψ is optimized using independently sampled frames. Given reference coverage C_i^* and reference tangent T_i^* , we define the foreground mask $M_i = \mathbb{I}(C_i^* > 0)$. The spatial coverage loss combines mean squared error (MSE) and L_1 loss on the foreground:

$$\mathcal{L}_{\text{cov}} = w_{\text{mse}} \text{mse}(C_i \odot M_i, C_i^*) + w_{L_1} L_1(C_i \odot M_i, C_i^*), \quad (9)$$

where and all losses are averaged over valid pixels unless otherwise stated. The support-mask loss combines binary cross-entropy (BCE)

and differentiable intersection over union (IoU) are defined as:

$$\mathcal{L}_{\text{mask}} = w_{\text{bce}} \text{bce}(\mathbf{L}_i, \mathbf{M}_i) + w_{\text{IoU}} \text{IoU}(\mathbf{L}_i, \mathbf{M}_i). \quad (10)$$

The tangent loss is a foreground-masked L_1 loss averaged over the three tangent channels:

$$\mathcal{L}_{\text{tan}} = \|(\mathbf{T}_i - \mathbf{T}_i^*) \odot \mathbf{M}_i\|_1 / 3 \sum \mathbf{M}_i. \quad (11)$$

The full spatial objective is

$$\mathcal{L}^s = w_{\text{cov}} \mathcal{L}_{\text{cov}} + w_{\text{mask}} \mathcal{L}_{\text{mask}} + w_{\text{tan}} \mathcal{L}_{\text{tan}}. \quad (12)$$

In the second stage, we freeze Ψ and train only the temporal network Γ on temporally ordered frame sequences. The temporal module is supervised using the same reference coverage, tangent, and support mask as in Eq. 12. The definitions of all loss functions are provided in the supplemental document.

5 Tangent-guided Reconstruction

The neural stage reconstructs coverage and tangent; however, reliable world-space positions are also required for deferred shading with shadows. As discussed above, the undersampled rasterized position map is often sparse and corrupted, and some hair pixels may lack valid position samples altogether. To address this issue, we introduce a tangent-guided reconstruction module that exploits local directional consistency in the reconstructed tangent field to recover world-space positions. Specifically, we design a bidirectional propagation strategy, consisting of backward repair and forward voting, to infer missing world-space positions while preserving anisotropic strand structures.

For each frame, the module takes as input a noisy world-space position map $\mathbf{P} \in \mathbb{R}^{H \times W \times 3}$, a noisy depth map $\mathbf{D} \in \mathbb{R}^{H \times W}$, the temporally reconstructed world-space tangent map $\mathbf{T}^t \in \mathbb{R}^{H \times W \times 3}$, the reconstructed coverage map $\mathbf{C}^t \in \mathbb{R}^{H \times W}$, and the view-projection matrix. Our goal is to recover a refined position map \mathbf{P}^* by combining backward repair for missing samples with forward voting from valid samples.

5.1 Pixel Classification

We first determine which pixels belong to the hair support and which of them contain valid position samples. A pixel \mathbf{p} is considered a hair pixel if its reconstructed coverage is positive. Among hair pixels, we classify \mathbf{p} as *valid* if its rasterized world-space position is available, and *invalid* otherwise. In practice, following the rasterization convention that missing positions are encoded as zeros, we use $\|\mathbf{P}(\mathbf{p})\| > \epsilon_{\text{pos}}$ as the validity criterion. Valid pixels may cast votes during reconstruction, whereas invalid pixels may only receive them.

5.2 Depth Inpainting

To support tangent-guided propagation at all hair pixels, we first fill missing depth values. For each hair pixel \mathbf{p} whose reconstructed coverage is positive but whose depth is missing, we copy the depth from its nearest valid neighbor in image space:

$$\mathbf{D}(\mathbf{p}) \leftarrow \mathbf{D}(\mathbf{p}^*), \quad \mathbf{p}^* = \arg \min_{\mathbf{q}: \mathbf{D}(\mathbf{q}) > 0} \|\mathbf{p} - \mathbf{q}\|_2. \quad (13)$$

This simple inpainting step ensures that every hair pixel is associated with a depth estimate for the subsequent geometric computations.

5.3 Bidirectional Position Reconstruction

Stage I. Per-pixel Step Size. We first estimate a local world-space step length for each pixel from the inpainted depth map and the camera intrinsics (f_x, f_y) . Specifically, we approximate the horizontal and vertical world-space displacements corresponding to one image-space pixel at depth $\mathbf{D}(\mathbf{p})$ as $\mathbf{D}(\mathbf{p})/f_x$ and $\mathbf{D}(\mathbf{p})/f_y$, respectively, and define

$$l_p = \sqrt{(\mathbf{D}(\mathbf{p})/f_x)^2 + (\mathbf{D}(\mathbf{p})/f_y)^2}. \quad (14)$$

Intuitively, l_p converts a one-pixel displacement in image space into an approximate world-space propagation step at pixel \mathbf{p} .

Stage II. Screen-space Curvature Center Estimation. For each hair pixel \mathbf{p} , we estimate a 2D curvature center \mathbf{c}_p in screen space by fitting a local circle to neighboring hair pixels within a 11×11 window, masked by the reconstructed coverage. The estimated curvature center provides a geometric prior for selecting the most plausible source sample when repairing a missing target pixel. The full implementation is provided in the supplemental material.

Stage III. Screen-space Tangent Projection. For each hair pixel \mathbf{p} , we project the reconstructed 3D tangent $\mathbf{T}^*(\mathbf{p})$ into the image plane using the view-projection matrix, and normalize the result to obtain a 2D screen-space tangent $\mathbf{T}_{\text{screen}}(\mathbf{p})$. This projected tangent captures the local strand direction in image space and is later used to determine whether a valid pixel should cast a vote toward a neighboring target pixel.

Stage IV. Backward Repair for Missing Pixels. For each invalid target pixel \mathbf{p} , we inspect its 3×3 neighborhood \mathcal{N}_p and select the valid neighbor \mathbf{s}^* whose curvature center is closest to that of \mathbf{p} :

$$\mathbf{s}^* = \arg \min_{\mathbf{s} \in \mathcal{N}_p \cap \mathcal{V}} \|\mathbf{c}_s - \mathbf{c}_p\|_2, \quad (15)$$

where \mathcal{V} denotes the set of valid pixels. We then initialize the missing world-space position by propagating from the selected source sample along the reconstructed tangent at the target pixel:

$$\mathbf{P}^*(\mathbf{p}) = \mathbf{P}(\mathbf{s}^*) + l_p \mathbf{T}^*(\mathbf{p}). \quad (16)$$

Since the tangent field is densely reconstructed by the neural stage, this strategy remains applicable even at pixels whose original position samples are missing.

Stage V. Forward Voting from Valid Pixels. Each valid pixel \mathbf{s} also casts votes toward neighboring pixels by projecting its world-space position forward along its tangent:

$$\mathbf{P}_{\mathbf{s} \rightarrow \mathbf{p}}^{\text{vote}} = \mathbf{P}(\mathbf{s}) + l_s \mathbf{T}(\mathbf{s}). \quad (17)$$

A vote from \mathbf{s} to a neighboring target pixel \mathbf{p} is accepted only if the screen-space tangent at \mathbf{s} is sufficiently aligned with the direction from \mathbf{s} to \mathbf{p} :

$$\left| \mathbf{T}_{\text{screen}}(\mathbf{s}) \cdot \frac{\mathbf{p} - \mathbf{s}}{\|\mathbf{p} - \mathbf{s}\|_2} \right| \geq \cos \theta_{\text{max}}, \quad (18)$$

where we set $\theta_{\text{max}} = 30^\circ$ in all experiments. Each target pixel \mathbf{p} maintains a candidate pool \mathcal{C}_p containing up to K accepted votes. When the pool is full, we discard the candidate with the largest

depth. The final forward estimate is then chosen as the frontmost candidate:

$$\mathbf{P}^*(\mathbf{p}) = \arg \min_{\mathbf{q} \in C_p} \text{depth}(\mathbf{q}), \quad (19)$$

where $\text{depth}(\mathbf{q})$ denotes the screen-space depth of a world-space position \mathbf{q} computed using the view-projection matrix. This visibility-aware selection suppresses implausible votes from deeper layers and favors the frontmost visible hair surface.

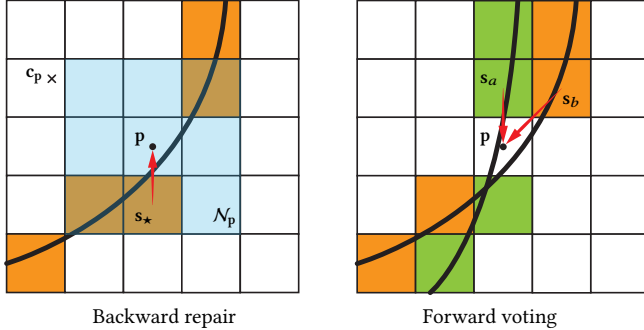


Fig. 3. Left: given an empty pixel \mathbf{p} with reconstructed tangent direction, we estimate its curvature center at \mathbf{c}_p . For its 3×3 neighborhood \mathcal{N}_p , we identify the neighbor \mathbf{s}_* whose curvature center is closest to \mathbf{c}_p and propagate it to \mathbf{p} . Right: from valid pixels \mathbf{s}_a and \mathbf{s}_b , which have already been marked as hair, we propagate along the tangent direction. For each reached missing pixel, we assign the value with the minimum depth.

Remark. The key observation behind our reconstruction strategy is that hair exhibits strong local directional coherence: neighboring pixels that belong to the same visible strand or strand bundle tend to follow a consistent tangent direction in screen space. Once coverage and tangent have been reliably reconstructed by the neural stage, this directional structure provides a strong cue for recovering missing geometric attributes. In particular, a missing position sample can often be inferred either by tracing backward from a nearby valid sample or by receiving a forward proposal from neighboring valid pixels along the local tangent direction. This motivates our bidirectional reconstruction strategy, which combines backward repair and forward voting to improve robustness under sparse rasterization.

For full details of our algorithm, we provide step-by-step pseudocode in the supplementary material.

6 Results

We train our network on a GPU with 14,592 cores and 96 GB of VRAM using a dataset generated in Unreal Engine. The dataset contains 1,000 samples from four hairstyles rendered under diverse conditions, including variations in camera viewpoint and distance, hair width, and hair dynamics. We apply sub-pixel jittering using a repeated 8-sample Halton sequence with bases 2 and 3. We pre-train the network for 40,000 iterations, which takes approximately 7 days, and then fine-tune it for 2,000 iterations for each hairstyle. During pre-training, the learning rate is adaptively decayed by a factor of 0.75 from 1×10^{-3} to 1×10^{-5} after 100 iterations, with no improvement in the loss. During fine-tuning, we use a smaller fixed learning

rate of 1×10^{-5} . We set $w_{\text{mse}} = 0.6$, $w_{L_1} = 0.4$, $w_{\text{bce}} = 0.7$, $w_{\text{IoU}} = 0.3$, $w_{\text{cov}} = 0.4$, $w_{\text{mask}} = 0.3$, and $w_{\text{tan}} = 0.3$ for all experiments. Unless otherwise specified, all experiments are conducted in Unreal Engine at a resolution of 1920×1080 on a desktop equipped with a GPU with 14,592 cores and 24 GB of VRAM, and an Intel i9-14900KF CPU. All timing reported is in milliseconds.

Comparison with Conventional and Industrial Learning-based Methods. We compare our method against conventional anti-aliasing baselines provided by Unreal Engine 5, including 8-spp MSAA, 4 \times SSAA, and TAA. MSAA uses 8 samples per pixel. SSAA renders at 2 \times resolution in both width and height and then downsamples the result to the target resolution. TAA accumulates 8 jittered frames using motion-vector-based history reprojection and default history clamping. We also compare our method against industrial learning-based methods, including DLSS 4 [NVIDIA 2025] and FSR [AMD 2021], integrated as plugins in Unreal Engine 5. For DLSS, we use DLAA mode without Ray Reconstruction or Frame Generation. For FSR, we use Native AA mode without sharpening or Frame Generation. We report MSE, PSNR, SSIM, LPIPS, and FLIP in Table 1 for the static hairstyle shown in Fig. 4. All metrics are computed only on pixels corresponding to hair in the reference image. Our method consistently outperforms all competing methods across all quantitative metrics. In terms of performance, our method is comparable to heavily engineered industrial solutions while requiring only 0.8 ms per frame, making it well-suited for practical use.

Table 1. Quantitative comparison on static hairstyles shown in Fig. 4.

Method	MSE↓	PSNR↑	SSIM↑	LPIPS↓	FLIP↓	Time↓ (ms)
Input	0.0318	14.97	0.9295	0.0573	0.0173	–
MSAA	0.0065	21.89	0.9264	0.0578	0.0168	2.0
SSAA	0.0177	17.52	0.9000	0.0932	0.0291	3.1
TAA	0.0102	19.92	0.9347	0.0591	0.0283	0.1
FSR	0.0124	19.07	0.9218	0.0772	0.0289	0.5
DLSS	0.0098	20.08	0.9338	0.0583	0.0289	0.5
Ours	0.0018	27.43	0.9659	0.0206	0.0073	0.8

Extremely curved hairstyle. We highlight the advantage of our geometry-aware G-buffer-based formulation on extremely curved or highly tangled hairstyles, such as the afro hair shown in Fig. 8 and the supplementary video.

These hairstyles contain rapidly changing strand directions, dense overlaps, and complex silhouettes, making them particularly challenging for RGB-space denoising methods. Since the final RGB image entangles coverage, visibility, depth ordering, shadows, and multiple scattering, directly filtering RGB values tends to blur fine curved strands or mix shading information from different depth layers. In contrast, our method performs reconstruction in G-buffer space before deferred shading. By first reconstructing coverage and tangent and then using them to guide position completion, our method preserves local strand directionality and maintains better consistency among coverage, tangent, and position. This geometry-aware reconstruction leads to clearer strand boundaries and more stable shading than RGB-based methods in highly curved hair regions.

Comparison with Academic Hair-specialized Methods. In addition to general denoising methods, we compare against a neural filtering

method specialized for hair rendering [Currius et al. 2022]. Their method assumes direct illumination with a simplified hair shading model. In contrast, our method targets a different low-sample strand-based rendering pipeline and reconstructs geometry-related G-buffers. As shown in Fig. 9 and Table 2, the method of Currius et al. [2022] improves the noisy input but tends to blur fine strands and produce less accurate shading in regions with complex strand overlap, which is particularly proved by the huge gap of the perceptual metric LPIPS (0.0622 vs our 0.0094). Moreover, because it uses transposed convolutions for upsampling in its decoder, the method of Currius et al. [2022] takes about 20 ms on an NVIDIA RTX 2060 GPU. By contrast, our G-buffer-based formulation preserves geometric consistency prior to shading, yielding sharper strand details, more accurate shadows and scattering, and improved quantitative performance on the same device. We also note a recent real-time hair filtering method by Huang et al. [2025b]. Unfortunately, its implementation is not publicly available. According to the paper, their method requires 8 ms per frame for hair containing 50,000 strands at a screen resolution of 1920×1080 . However, the paper does not report the hardware specifications or quantitative evaluation metrics. Under the same setup, their reported runtime is roughly $10\times$ slower than ours, which is reasonable because their analytic hair-linking approach requires explicit pixel-hair intersection tests.

Table 2. Quantitative comparison with [Currius et al. 2022]. Note that the results of Currius et al. [2022] with their best model and ours for timing on the table were obtained on an Nvidia RTX 2060.

Method	MSE↓	PSNR↑	SSIM↑	LPIPS↓	FLIP↓	Time↓ (ms)
Currius et al. [2022]	0.0033	24.78	0.9251	0.0622	0.0247	20.3
Ours	0.0010	30.06	0.9832	0.0094	0.0105	3.6

Dynamic Hairs. To evaluate temporal stability, we further test our method on dynamic hair simulation sequences (Fig. 5). Unlike static scenes, dynamic scenes introduce temporal changes, disocclusions, and frame-to-frame sampling variation, making flickering and ghosting more noticeable. In addition to spatial metrics, we include the perceptual video metric FVVD [Mantiuk et al. 2021] to assess spatiotemporal artifacts, such as flicker and judder. Table 3 highlights that our method consistently outperforms all competing methods across all quantitative metrics while maintaining a performance cost comparable to that of industrial solutions.

Table 3. Quantitative metrics on dynamic hairs on Fig. 5.

Method	MSE↓	PSNR↑	SSIM↑	LPIPS↓	FLIP↓	FVVD↑	Time↓ (ms)
Input	0.0111	19.72	0.9433	0.0513	0.0192	8.42	–
TAA	0.0067	21.83	0.9706	0.0269	0.0181	8.11	0.2
FSR	0.0068	21.74	0.9642	0.0291	0.0180	8.14	0.8
DLSS	0.0059	22.37	0.9680	0.0267	0.0175	8.21	0.7
Ours	0.0015	28.57	0.9756	0.0155	0.0075	9.27	1.0

More Evaluations. We further evaluate our method under different lighting configurations, including front, side, and back lighting, as well as across different hair colors. Because our method reconstructs the rasterized hair G-buffer, it naturally supports such variations,

as shown in Fig. 7. We also compare performance across a variety of hairstyles, including straight, wavy, curly, and afro hair, shown in Fig. 4, which exhibit different strand densities, curvatures, and silhouette complexities. The results demonstrate that our method can recover the spatial structure of hair, reduce aliasing, and produce images that are closer to the high-sample reference. More quantitative comparisons are provided in the supplemental document.

Ablation Study on Proposed Components. To evaluate the contribution of each major component in our pipeline, we perform an ablation study of the spatial module, temporal module, and tangent-guided reconstruction. In summary, as shown in Fig. 6, removing any component degrades the final rendering quality. Without the spatial module, the result preserves the overall hair structure but contains more residual noise and less accurate fine-strand details. Removing temporal accumulation reduces both reconstruction accuracy and temporal stability under dynamic hair motion. Interestingly, directly shading the reconstructed coverage and tangent produced by our spatiotemporal module while using noisy positions leads to even larger errors, due to misalignment among coverage, tangent, and position, which in turn causes incorrect shadows and multi-bounce scattering. Our neural spatiotemporal modules and tangent-guided reconstruction are complementary. The neural modules improve the quality and temporal stability of coverage and tangent, while tangent-guided reconstruction aligns the position with the reconstructed G-buffers, which is essential for robust deferred shading. A quantitative comparison is provided in the supplemental document.

Performance. We measure the performance of all experiments using NVIDIA Nsight. As an example, our spatial module, temporal accumulation, and analytic filtering take 0.6 ms, 0.3 ms, and 0.1 ms, respectively, for a total of 1.0 ms. The cost scales proportionally with the screen resolution.

7 Conclusion

We have presented a lightweight, real-time neural hair denoising pipeline for reconstructing severely undersampled strand-based hair G-buffers prior to deferred shading. Our method reconstructs the G-buffers by restoring coverage and tangent with neural spatiotemporal modules and completing position with a tangent-guided reconstruction module. This design preserves the geometric consistency required for physically based hair shading and avoids directly correcting errors that are already entangled with visibility, lighting, shadows, and scattering.

Limitations. Our method has several limitations. First, our neural modules are limited by the training data. For hairstyles whose geometric characteristics differ substantially from those seen during training, the network may generalize less effectively. For applications that require high-precision reconstruction of a specific hairstyle, fine-tuning the network on that hairstyle or on a closely matched dataset may be beneficial. Second, while our method runs in real time, it remains slightly slower than highly optimized industrial methods such as DLSS and FSR. Our current implementation prioritizes algorithmic clarity and research validation rather than low-level engine optimization. With further engineering optimizations, such as kernel fusion and platform-specific acceleration, the

runtime could be further reduced. In addition, because our method denoises geometry-related G-buffers rather than RGB color, its output can be cached and reused when the camera and hair geometry are static. Thus, for lighting-only changes, we can avoid repeated denoising and simply re-shade the reused denoised G-buffers, saving additional runtime. This is a unique advantage over RGB-based methods, whose denoising inputs vary with illumination.

References

- AMD. 2021. AMD FidelityFX Super Resolution. <https://gpuopen.com/fidelityfx-superresolution/>. Accessed: 2026-04-03.
- Gaurav Bhokare, Eisen Montalvo, Elie Diaz, and Cem Yuksel. 2024. Real-Time Hair Rendering with Hair Meshes. In *ACM SIGGRAPH 2024 Conference Papers* (Denver, CO, USA) (SIGGRAPH '24). Association for Computing Machinery, New York, NY, USA, Article 61, 10 pages.
- Matt Jen-Yuan Chiang, Benedikt Bitterli, Chuck Tappan, and Brent Burley. 2016. A Practical and Controllable Hair and Fur Model for Production Path Tracing. *Comput. Graph. Forum* 35, 2 (2016), 275–283.
- Roc R. Currius, Ulf Assarsson, and Erik Sintorn. 2022. Real-Time Hair Filtering with Convolutional Neural Networks. *Proc. ACM Comput. Graph. Interact. Tech.* 5, 1, Article 15 (May 2022), 15 pages.
- Tri Dao, Daniel Y. Fu, Stefano Ermon, Atri Rudra, and Christopher Ré. 2022. FLASHATTENTION: fast and memory-efficient exact attention with IO-awareness. In *Proceedings of the 36th International Conference on Neural Information Processing Systems* (New Orleans, LA, USA) (NIPS '22). Curran Associates Inc., Red Hook, NY, USA, Article 1189, 16 pages.
- Eugene d'Eon, Guillaume François, Martin Hill, Joe Letteri, and Jean-Marie Aubry. 2011. An Energy-Conserving Hair Reflectance Model. *Comput. Graph. Forum* 30, 4 (2011), 1181–1187.
- Anitha Edison and C.V. Jiji. 2017. Optical Acceleration for Motion Description in Videos. In *2017 IEEE Conference on Computer Vision and Pattern Recognition Workshops (CVPRW)*. IEEE, New Brunswick, NJ, USA, 1642–1650.
- Epic Games. 2021. Unreal Engine. <https://www.unrealengine.com>
- Xihao Fu. 2023. Better Real-Time Strand-Based Hair Rendering with Ray Tracing. <https://www.nvidia.com/en-us/on-demand/session/gtc-spring23-s51709/> NVIDIA GPU Technology Conference (GTC 2023).
- Tao Huang, Haoyang Shi, Mengdi Wang, Yuxing Qiu, Yin Yang, and Kui Wu. 2025a. Real-Time Knit Deformation and Rendering. *ACM Trans. Graph.* 44, 4, Article 52 (July 2025), 12 pages.
- Tao Huang, JunPing Yuan, Ruike Hu, Lu Wang, Yanwen Guo, Bin Chen, Jie Guo, and Junqiu Zhu. 2025b. Detail-Preserving Real-Time Hair Strand Linking and Filtering. *Computer Graphics Forum* 44, 4 (2025), 11 pages.
- T. Huang, Y. Zhou, D. Lin, J. Zhu, L. Yan, and K. Wu. 2025c. Real-time Level-of-detail Strand-based Rendering. *Computer Graphics Forum* 44, 4 (2025), e70181.
- W. Huang, M. B. Hullin, and J. Hanika. 2022. A Microfacet-based Hair Scattering Model. *Computer Graphics Forum* 41, 4 (2022), 79–91.
- Yibing Jiang. 2016. The process of creating volumetric-based materials in uncharted 4. *Siggraph Courses: Advances in Real-Time Rendering in Games, Anaheim, CA* 0, 0 (2016), 0.
- J. T. Kajiya and T. L. Kay. 1989. Rendering Fur with Three Dimensional Textures. *SIGGRAPH Comput. Graph.* 23, 3 (jul 1989), 271–280.
- Javor Kalojanov and Kimball Thurston. 2023. Robust Average Networks for Monte Carlo Denoising. arXiv:2310.04080 [cs.GR] doi:10.48550/arXiv.2310.04080
- Pramook Khungurn and Steve Marschner. 2017. Azimuthal Scattering from Elliptical Hair Fibers. *ACM Trans. Graph.* 36, 2, Article 13 (apr 2017), 23 pages.
- Chuan Koon Koh and Zhiyong Huang. 2001. A Simple Physics Model to Animate Human Hair Modeled in 2D Strips in Real Time. In *Proceedings of the Eurographic Workshop on Computer Animation and Simulation* (Manchester, UK). Springer-Verlag, Berlin, Heidelberg, 127–138.
- Aakash KT, Adrian Jarabo, Carlos Aliaga, Matt Jen-Yuan Chiang, Olivier Maury, Christophe Hery, P. J. Narayanan, and Giljoon Nam. 2023. Accelerating Hair Rendering by Learning High-Order Scattered Radiance. *Computer Graphics Forum* 42, 4 (2023), e14895.
- Sergei Kulikov. 2015. Strand-based hair and fur rendering in Indiana Jones and the Great Circle. *ACM SIGGRAPH Courses: Advances in Real-Time Rendering in Games Course* 0, 0 (2015), 0.
- Timothy Lottes. 2009. Fast Approximate Anti-Aliasing (FXAA). https://developer.download.nvidia.com/assets/gamedev/files/sdk/11/FXAA_WhitePaper.pdf.
- Rafal K. Mantiuk, Gyorgy Denes, Alexandre Chapiro, Anton Kaplanyan, Gizem Rufo, Romain Bachy, Trisha Lian, and Anjul Patney. 2021. FovVideoVDP: a visible difference predictor for wide field-of-view video. *ACM Trans. Graph.* 40, 4, Article 49 (July 2021), 19 pages.
- Stephen R. Marschner, Henrik Wann Jensen, Mike Cammarano, Steve Worley, and Pat Hanrahan. 2003. Light scattering from human hair fibers. *ACM Trans. Graph.* 22, 3 (2003), 780–791.
- Zahra Montazeri, {Soren B.} Gammelmark, {Henrik Wann} Jensen, and Shuang Zhao. 2021. A Practical Ply-Based Appearance Modeling for Knitted Fabrics. In *Eurographics Symposium on Rendering*.
- Zahra Montazeri, Søren B. Gammelmark, Shuang Zhao, and Henrik Wann Jensen. 2020. A Practical Ply-Based Appearance Model of Woven Fabrics. *ACM Trans. Graph.* 39, 6, Article 251 (nov 2020), 13 pages.
- Jonathan T. Moon and Stephen R. Marschner. 2006. Simulating multiple scattering in hair using a photon mapping approach. *ACM Trans. Graph.* 25, 3 (2006), 1067–1074.
- Jonathan T. Moon, Bruce Walter, and Steve Marschner. 2008. Efficient Multiple Scattering in Hair Using Spherical Harmonics. In *ACM SIGGRAPH 2008 Papers* (Los Angeles, California) (SIGGRAPH '08). Association for Computing Machinery, New York, NY, USA, Article 31, 7 pages.
- NVIDIA. 2025. DLSS 4: Transforming Real-Time Graphics with AI. <https://research.nvidia.com/labs/adlr/DLSS4>. Accessed: 2026-04-03.
- Iman Sadeghi, Heather Pritchett, Henrik Wann Jensen, and Rasmus Tamstorf. 2010. An Artist Friendly Hair Shading System. In *ACM SIGGRAPH 2010 Papers* (Los Angeles, California) (SIGGRAPH '10). Association for Computing Machinery, New York, NY, USA, Article 56, 10 pages.
- Sebastian Tafuri. 2019. Strand-based Hair Rendering in Frostbite. *ACM SIGGRAPH Courses: Advances in Real-Time Rendering in Games Course* 0, 0 (2019), 0.
- Thijs Vogels, Fabrice Rousselle, Brian McWilliams, Gerhard Röhlin, Alex Harvill, David Adler, Mark Meyer, and Jan Novák. 2018. Denoising with kernel prediction and asymmetric loss functions. *ACM Trans. Graph.* 37, 4, Article 124 (July 2018), 15 pages.
- Kui Wu and Cem Yuksel. 2016. Real-time hair mesh simulation. In *Proceedings of the 20th ACM SIGGRAPH Symposium on Interactive 3D Graphics and Games* (Redmond, Washington) (ISD '16). Association for Computing Machinery, New York, NY, USA, 59–64.
- Mengqi Xia, Bruce Walter, Christophe Hery, Olivier Maury, Eric Michielssen, and Steve Marschner. 2023. A Practical Wave Optics Reflection Model for Hair and Fur. *ACM Trans. Graph.* 42, 4, Article 39 (jul 2023), 15 pages.
- Mengqi (Mandy) Xia, Bruce Walter, Eric Michielssen, David Bindel, and Steve Marschner. 2020. A Wave Optics Based Fiber Scattering Model. *ACM Trans. Graph.* 39, 6, Article 252 (nov 2020), 16 pages.
- Ling-Qi Yan, Chi-Wei Tseng, Henrik Wann Jensen, and Ravi Ramamoorthi. 2015. Physically-Accurate Fur Reflectance: Modeling, Measurement and Rendering. *ACM Trans. Graph.* 34, 6, Article 185 (nov 2015), 13 pages.
- Lei Yang, Shiqiu Liu, and Marco Salvi. 2020. A Survey of Temporal Antialiasing Techniques. *Computer Graphics Forum* 39, 2 (2020), 607–621.
- Cem Yuksel and John Keyser. 2008. Deep Opacity Maps. *Computer Graphics Forum (Proceedings of EUROGRAPHICS 2008)* 27, 2 (2008), 675–680.
- Cem Yuksel, Scott Schaefer, and John Keyser. 2009. Hair meshes. *ACM Trans. Graph.* 28, 5 (Dec. 2009), 1–7.
- Junqiu Zhu, Zahra Montazeri, Julien Aubry, Ling-Qi Yan, and Andrea Weidlich. 2023. A Practical and Hierarchical Yarn-based Shading Model for Cloth. *Computer Graphics Forum* 42, 4 (July 2023), 2–11.
- Junqiu Zhu, Sizhe Zhao, Lu Wang, Yanning Xu, and Ling-Qi Yan. 2022. Practical level-of-detail aggregation of fur appearance. *ACM Trans. Graph.* 41, 4 (2022), 47:1–47:17.
- Arno Zinke, Martin Rump, Tomás Lay, Andreas Weber, Anton Andriyenko, and Reinhard Klein. 2009. A practical approach for photometric acquisition of hair color. *ACM Trans. Graph.* 28, 5 (2009), 165.
- Arno Zinke, Cem Yuksel, Andreas Weber, and John Keyser. 2008. Dual scattering approximation for fast multiple scattering in hair. *ACM Trans. Graph.* 27, 3 (2008), 32.

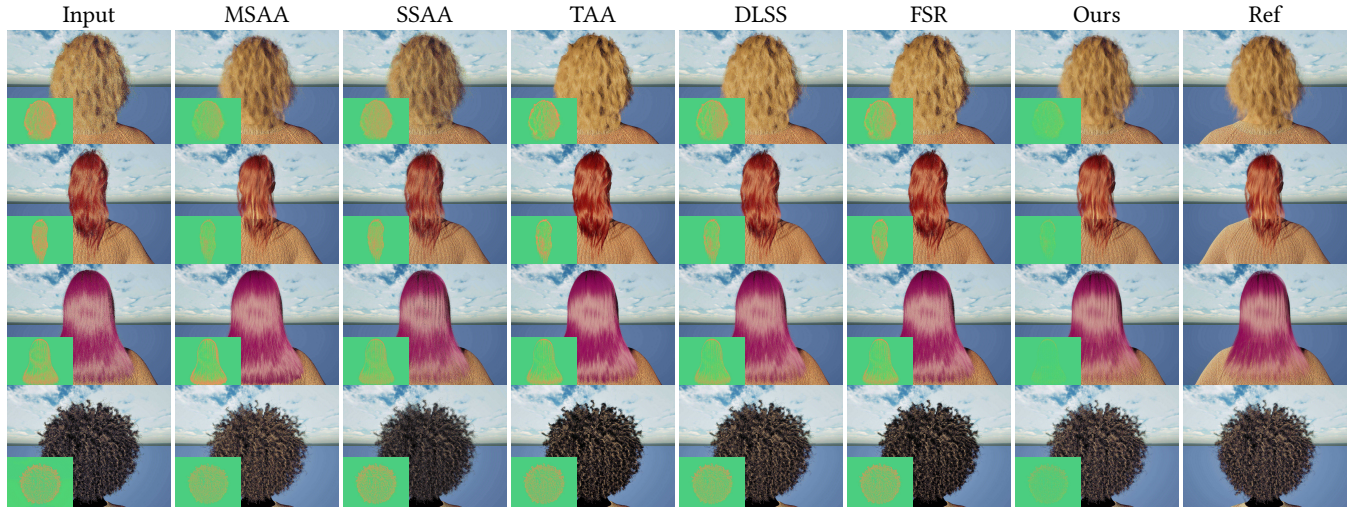


Fig. 4. Comparisons on different static hairstyles. The bottom-left corner shows the error map.

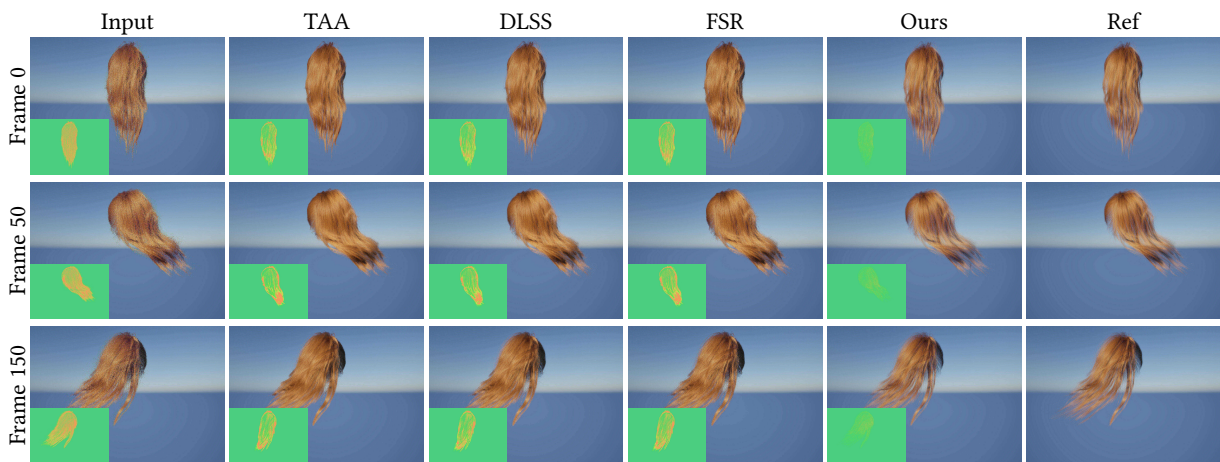


Fig. 5. Comparison on dynamic hair sequence.

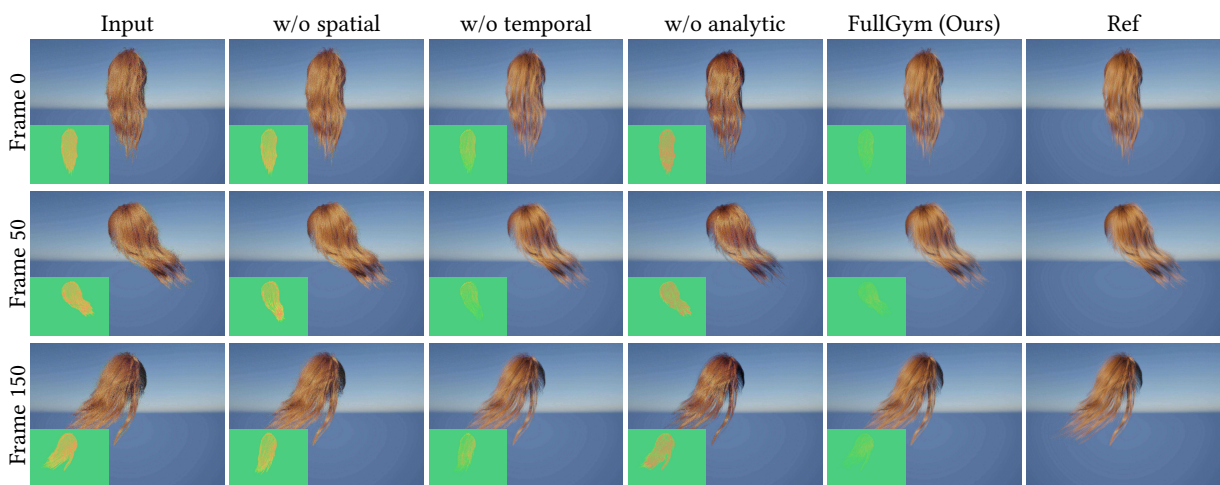


Fig. 6. Ablation studies on components of our method. The corresponding quantitative comparison is provided in the supplemental document.

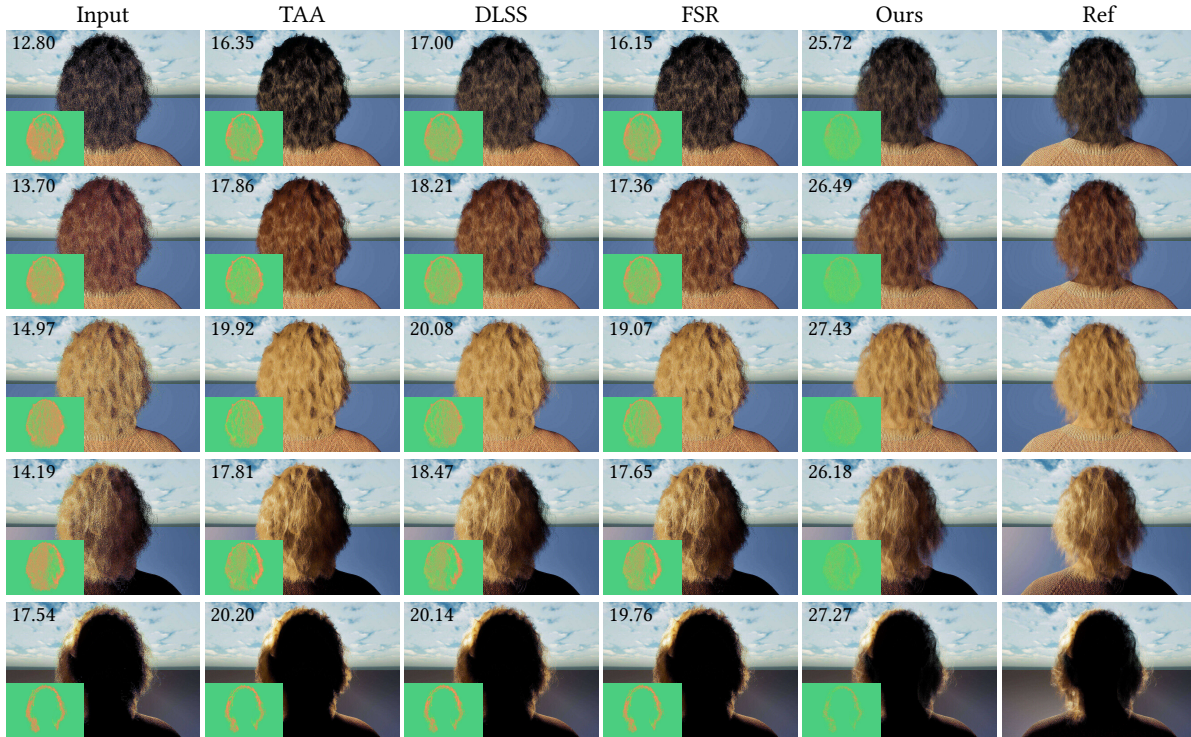


Fig. 7. Different color and lighting. The bottom-left corner shows the error map. Our method remains robust and yields the smallest error across different hair colors and lighting conditions, as it operates on G -buffers. The top-left number indicates the corresponding PSNR relative to the reference.



Fig. 8. Zoom in comparison of extremely curved and highly tangled hairstyle under back lighting. These results demonstrate the benefit of reconstructing geometry-related G -buffers before shading, rather than directly filtering the final RGB image.

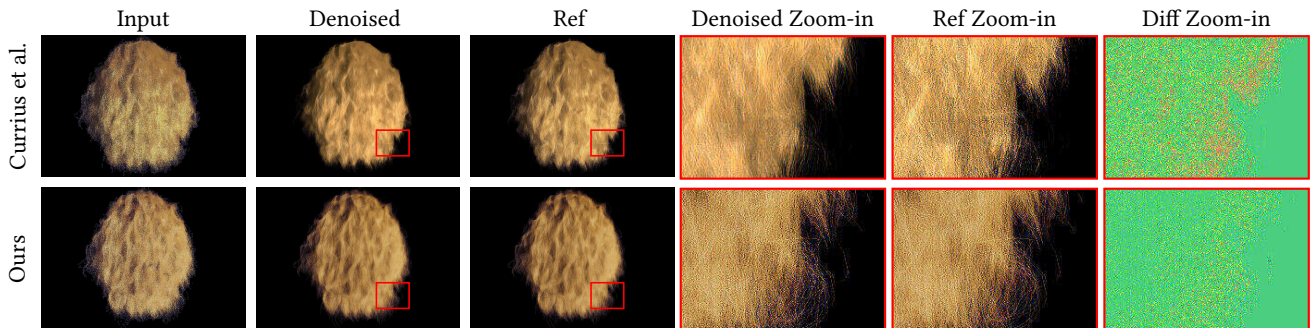


Fig. 9. Comparison with the neural hair denoiser of Currius et al. [2022] on the same scene. Note that the input and reference images differ from ours because their method uses a different hair-shading model with direct illumination. Their method produces less accurate and blurred shading in regions with complex strand overlap, leading to a much larger perceptual error as measured by LPIPS (0.0622 versus our 0.0094).